

An Improved Hyperbolic Method and Its Application to Property Inversion in Martian Tianwen-1 GPR Data

Renrui Liu[✉], Yi Xu[✉], Member, IEEE, Ruonan Chen, Jiannan Zhao[✉], and Xiaoting Xu

Abstract—On May 15, 2021, the Tianwen-1 (TW-1) successfully landed on the surface of Mars within the southern Utopia Planitia (UP). It delivered a rover named Zhurong equipped with ground penetrating radar (GPR), a device that can investigate the thickness and structure of the geological layers below the Martian surface. The hyperbola method is commonly used for extracting dielectric property variations with depth from GPR data to aid the interpretation of the subsurface structure and material composition. This study analyzes the advantages and drawbacks of three hyperbola methods with different geometric models. Next, it proposes a new method aiming to use the highly precise, yet complex geometric model and address issues caused by its solving process. We also analyze the influencing factors contributing to measurement errors and design corresponding criteria for measurement point selection to mitigate errors. The average error of the proposed method is less than 5% for a depth of up to 9 m. We employed the proposed method to obtain the dielectric constant distribution in the shallow surface layer of the TW-1 landing zone to a depth of up to 16 m. The dielectric constant is mainly concentrated between 2 and 8 m and increases gradually with depth. Below 2 m, the dielectric constant is about 5.1 and the density is about 2.5 g/cm³. The stratification and density variation can be inferred from the dielectric constant distribution diagram.

Index Terms—constant, ground penetrating radar (GPR), Mars, Tianwen-1 (TW-1).

I. INTRODUCTION

ROUND-PENETRATING radar (GPR) data can reveal the subsurface structure of the composition, density, and water/ice content of the Martian ubiquitous weathering

Manuscript received 5 November 2022; revised 15 March 2023 and 17 April 2023; accepted 19 April 2023. Date of publication 26 April 2023; date of current version 10 May 2023. This work was supported in part by the National Key Research and Development Program under Grant 2021YFA0716100, in part by the Pre-Research Project on Civil Aerospace Technologies of China National Space Administration under Grant D020101, in part by the Science and Technology Development Fund of Macau under Grant 0049/2020/A1, and in part by the Guangdong–Hong Kong–Macao Greater Bay Area International Scientific and Technological Innovation Cooperation Project under Grant 2021A0505030080. (*Corresponding author:* Yi Xu.)

Renrui Liu, Yi Xu, and Xiaoting Xu are with the State Key Laboratory of Lunar and Planetary Sciences, Macau University of Science and Technology, Macau, China (e-mail: liurenruis@gmail.com; yixu@must.edu.mo; 2009853nse30001@student.must.edu.mo).

Ruonan Chen is with the Temasek Laboratories, National University of Singapore (NUS), Singapore 119077 (e-mail: rnchen@nus.edu.sg).

Jiannan Zhao is with the State Key Laboratory of Geological Processes and Mineral Resources, Planetary Science Institute, School of Earth Sciences, and the Key Laboratory of Geological Survey and Evaluation, Ministry of Education, China University of Geosciences, Wuhan 430074, China (e-mail: jnzhao@cug.edu.cn).

Digital Object Identifier 10.1109/TGRS.2023.3270518

layer [1], [2]. The information will help select sampling locations for the analysis of the potential past life forms on Mars and advance our understanding of its climate history, geological genesis, habitability, the exploration of Martian resources, and the construction of settlements on the planet [3], [4].

On May 15, 2021, China’s Tianwen-1 (TW-1) lander carrying the Zhurong rover successfully landed on Utopia Planitia (UP) in the northern lowlands of Mars (109.925 °E, 25.066 °N). The rover is equipped with the Mars Rover Penetrating Radar (RoPeR) for nondestructive measurement of the Martian subsurface environment [5].

The TW-1 landing area, UP is an ancient impact basin with a diameter of over 3300 km. After a long geological phase of weathering, deposition, and transportation, the surface has been mantled with a thick layer of mixed fillers [6]. The overall surface of the UP is smooth but also has distinct geological features, such as crenulated ridges, lobate margins, troughs, and so on [7]. Several interpretations have been proposed for the genesis of these geological features, some related to Martian groundwater and surface activity [8].

Before in situ measurements, orbiting GPRs led to important scientific discoveries of the Martian subsurface structure. The Mars advanced radar for subsurface and ionospheric sounding (MARSIS) carried by the Mars Express and can survey the Martian subsurface in the frequency range of 1.3–5.5 MHz [9]. MARSIS data have been used to obtain the distribution of the dielectric constant on the surface of Mars, which provides evidence for the existence of a Late Hesperian Ocean in the UP region [10]. SHallow RADar (SHARAD) operates at 20 MHz and has a higher range resolution than MARSIS, and the data can be used to derive the dielectric constant distribution of relatively shallow surfaces [11]. SHARAD data confirmed the presence of shallow water ice in the western UP [1].

As glimpsed from Zhurong’s panoramic camera, the terrain near the TW-1 landing area appears flat and relatively smooth. No large-scale rock is protruding on the surface and the dust-mantling layer obscures geomorphological information about the underlying rocks [12]. This weathering layer is relatively thin compared to the wavelength of the orbiter radars and cannot be observed, whereas the RoPeR operates from the surface without interference from the ionosphere and has a higher resolution for the analysis of the shallow surface.

The in situ GPR experiments performed on the lunar surface have been successfully utilized to extract the subsurface stratigraphy within a few hundred meters and this provides the

bases for processing the RoPeR data. Lai et al. [13] inferred information on the layer thickness, dielectric constant ϵ , density, loss tangent, and chemical components of the regolith using lunar penetrating radar (LPR) data from the Chang'E-4 and Chang'E-3 missions. Dong et al. [14] also used the hyperbolic method to extract the parabolic-shaped diffractions (PSDs) of LPR data to obtain the dielectric constant ϵ , density versus depth. By considering the height of the radar antenna, Fa [15] improved the dielectric constant inversing method using PSD. On this basis, Wang et al. [16] considered the antenna spacing to further improve the accuracy of the geometrical modeling of the method. The hyperbolic method has also been used to calculate the dielectric coefficient of the apparent PSD for other Martian GPR data, including "RIMFAX," the GPR carried by the Perseverance rover, launched at around the same time as TW-1 [17], [18].

GPR technology has been extensively used in engineering measurements on Earth. These measurements include determining the water and salt content, soil density, and so on, which require the derivation of the dielectric constant [19], [20]. One of the commonly used methods to calculate it is the hyperbolic method. The underground objects are represented as hyperbolic shapes in the GPR B-scan data, and by fitting the hyperbolic shape, the dielectric constant of the ground medium can be calculated [21].

In buried circular pipe detection, the cross section of the underground target appears as a positive circular shape in the radar image. By combining the circular formula with the hyperbolic formula, an algorithm for analyzing the ground-coupled GPR hyperbola was developed to calculate the dielectric constant of the ground medium, along with the radius and depth of the circular pipe and the hyperbolic shape [22], [23].

However, the hyperbolic formula of the air-coupled model is more complicated than the ground-coupled model and it is difficult to solve even without considering the shape of underground objects. Researchers have proposed various methods to address this issue, such as deriving a solution procedure for the nonstandard hyperbola using a generalized solution of the fourth-degree algebraic equation, which is computationally intensive [24]. Another proposed method involves using an approximation formula for nonstandard hyperbolas, which introduces a small error but is easier to solve [25], [26], [27].

In planetary exploration, the GPR instrument is often air-coupled and the subsurface objects are in nonstandard form, which makes it challenging to apply the aforementioned methods. Moreover, obtaining accurate results from data with a low signal-to-noise ratio (SNR) collected on the surface of a planetary body introduces additional challenges to the method design [28], [29].

In this work, we propose a new approach that considers the effects of antenna placements and object scale, addresses the issue of nonunique solutions of the inversing equations, and reduces the uncertainties caused by the calculation process. The Zhurong rover traveled 1280 m during ~ 191 Martian days [see Fig. 1(a)]. The high-frequency (HF) data of the RoPeR were processed and analyzed to obtain the dielectric constant profile of the shallow subsurface in the UP. The dielectric

characteristics and their geologic implications in the TW-1 landing area have been discussed.

II. METHODOLOGY AND MATERIALS

A. RoPeR Data and TW-1 Landing Region

The main scientific objective of the RoPeR is to characterize the thickness and sublayer distribution of the Martian soil [30]. RoPeR uses two channels: a low-frequency (LF) CH1 channel operating at 15–95 MHz and an HF CH2 channel operating between 0.45 and 2.15 GHz. The CH1 channel has a range resolution of several meters, while the HF has a higher resolution of several centimeters. The data used in this article are the CH2 data of the RoPeR. The antenna height of CH2 Tx is 0.345 m, Rx is 0.306 m, respectively, and the antenna spacing is 0.42 m (see Fig. 2) [30]. The sampling interval between two neighboring tracks of CH2 is 0.05 m. The GPR data are saved as traces, and each trace of CH2 is composed of 2048 data points with a time window of 235 ns. Since November 26, 2021, the Zhurong has traveled 1280 m [see Fig. 1(a)]. In the HiRISE image of the TW-1 landing region, the color around the landing site is darker than other areas due to the influence of the jet plume during the landing process. The Zhurong rover drove past several dunes, severely degraded craters, and small rocks throughout its travel route. The elevation gradually decreases from the northwest to the southeast direction [see Fig. 1(b)]. Fig. 1(c) shows the elevation data recorded during the movement of the rover. The whole area is relatively flat and the height difference of the traversing path does not exceed 7 m. After removing duplicate traces, a total of 22 840 RoPeR data traces were acquired. Next, data traces were aggregated into a $22\ 840 \times 2048$ data matrix, which is the B-scan data. A series of signal processing procedures, such as direct current (dc) removing, background removal, and filtering, were applied to improve the SNR of the acquired raw GPR data.

The Zhurong rover is designed to select a flat route to prevent rolling over. Figs. 1(c) and 2 show no obvious bumps or obstacles present on the surface of the traversing path. Also, whereas we observed large changes in surface echo strength, such as intensity anomalies that might be caused by surface roughness, we did not select the corresponding hyperbola signals to mitigate the uncertainties caused by surface unevenness.

B. Related Methods

1) *Traditional Hyperbola Method:* There are three mainstream methods for calculating the dielectric constant by PSD. The traditional and simplest method can obtain ϵ using (1), but it omits the influences of the antenna height and spacing [see Fig. 3(a)]

$$\epsilon = \frac{c^2(t^2 - t_0^2)}{4x^2}. \quad (1)$$

x and t are the horizontal location of a point in the hyperbola and its two-way traveling time, respectively. The dielectric constant ϵ is determined by measuring the vertex position (x_0, t_0) of the PSD in the B-scan image and the positions of

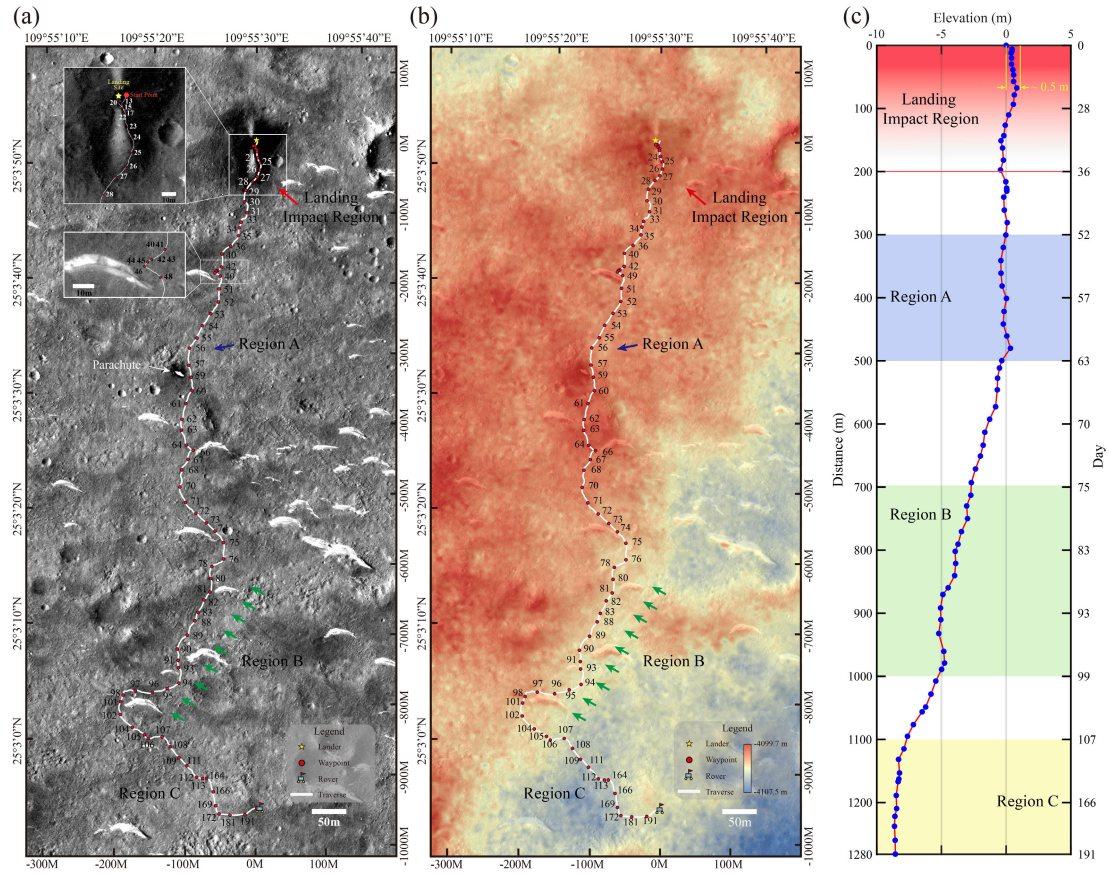


Fig. 1. (a) Zhurong rover's travel track and HiRISE image with the landing region. (b) DEM of the landing region. (c) Elevation data for the rover travel.

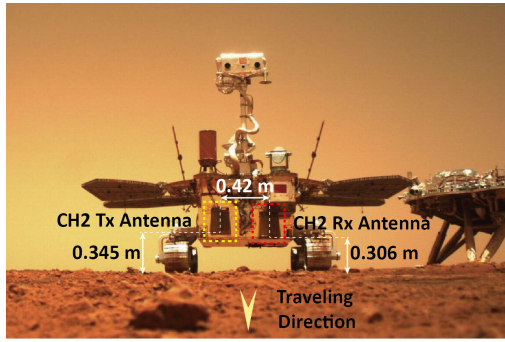


Fig. 2. Positions of the CH2 antennas on the rover.

the other measurement points (x, t) in the hyperbola. c in (1) is the speed of light. The algorithm has been widely used to calculate the dielectric constant of the PSD for B-scan data, e.g., the CE-3 and CE-4 LPR data [13], [14], [31]. The depth calculated by this method has an average error of 13.3% caused by measurement uncertainty [31], which is obtained with the finite-difference time-domain (FDTD) simulation results. However, the simulation model does not consider the antenna height and antenna spacing. Hence, the error of the actual measurement could be larger than the reported one.

The advantages of this method are that it is simple, easy to solve, and has a unique solution. In the process of fitting, the vertex position can be determined as the fitting variable to be

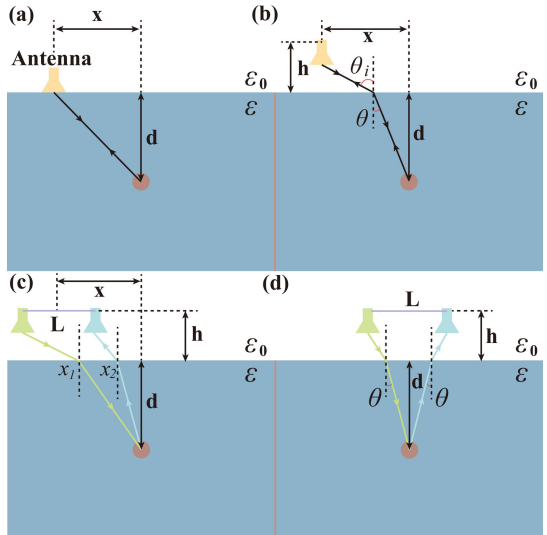


Fig. 3. (a) Model without considering antenna height and spacing. (b) Model where antenna height is considered but not antenna spacing. (c) Model where both antenna height and antenna spacing are considered. (d) Model considers the antenna height and antenna spacing when the rover travels directly above the object.

solved. Thus, the equation can be solved without knowing the vertex position and does not introduce additional errors.

However, the antenna height is not considered in (1), leading to the underestimation of the dielectric constant ε . The error of the dielectric constant calculated by this method is mainly introduced in the geometric model building.

2) Hyperbola Method Considering Antenna Height:

$$R = h \sec \theta_i + d \sqrt{\varepsilon} \sec \theta \quad (2)$$

$$\frac{R^2}{\varepsilon d^2} - \frac{x^2}{d^2} = 1 + \frac{2 \cos \theta_i}{\sqrt{\varepsilon - \sin^2 \theta_i}} \frac{h}{d} + \frac{1 - \varepsilon \sin^2 \theta_i}{\varepsilon \cos^2 \theta_i} \frac{h^2}{d^2}. \quad (3)$$

The second method considers the antenna height h in the model [see Fig. 3(b)] [15], which will result in $\pm 10\%-20\%$ change in the calculation result of dielectric constant ε . The maximum modification can reach 30% in the model of the Yutu-1 rover, where the antenna height is comparable to the half-wavelength of the GPR signal.

This model consists of (2) and (3), where d is the depth of the reflector, θ_i is the incidence angle, and θ is the transmission angle. The apparent range $R = ct/2$ of the electromagnetic wave propagation can be calculated using (2). Equation (3) gives the relationship between R and x , which is complex to solve. The solution of (3) is obtained by first calculating it in the forward direction with various settings of parameters, then generating a data table, and finally determining the results by looking up the table. The PSD curve can be generated with the dielectric constant ε and the depth d . Then, the eccentricity and the vertex position of the curve are obtained to represent the shape of the hyperbola. Using the forward calculation, a table can be obtained that records the vertex position and eccentricity of the PSD corresponding to different dielectric constants and depths. When measuring the PSD in the B-scan data and matching it with data in the table, the corresponding ε and d can be found using the vertex position and eccentricity of the PSD.

The algorithm improves the accuracy of results by modeling the antenna's height but introduces errors in the equation solving. The error originates from two aspects: the first is the selection of the vertex position, where the deviation of the vertex position leads to an error of the estimated ε . The second is the eccentricity of the hyperbola, depending on the clearness of the hyperbola in the radar image. For example, the defective or incomplete hyperbola due to interferences of other scatters or the intermittent data collection process will cause deviations in calculating the eccentricities. The main cause for these two errors is that the vertex position and eccentricity cannot represent the real shape of the PSD well, while the first method does not require these two parameters. Traditional methods of solving nonlinear equations use optimization algorithms, such as the Nelder–Mead or Gauss–Newton iteration method, the steepest descent method, and so on [32], [33]. They have the drawbacks of nonunique, local optimal solutions and deviations caused by the inapposite setting of the initial values [34], [35]. Compared to the traditional methods, the lookup table used here has relatively high computation complexity, but it is beneficial to the precision of the result. Modifying the description method of the PSD shape will further improve the accuracy of the solution.

3) Hyperbola Method Considering Height and Spacing of Antenna: The third algorithm models additional details by considering antenna spacing [see Fig. 3(c) and (d)] [16]. The estimated value can be obtained by solving (4)–(8). However, the calculation is the most complex among the three

approaches. The dielectric constant ε is solved by including the positions of the vertex and one of the measurement points of the PSD in equations. Each measurement point in the PSD corresponds to an independent solution of the dielectric constant. Finally, the average value of these dielectric constants is used as the estimated ε .

This algorithm also introduces uncertainties. First, the errors are caused by the selection of the vertex position. The second is that the equation has nonunique solutions when solved. Third, averaging the dielectric constants by calculating multiple measurement points can also introduce errors in the results. If the measurement points result in dispersed distribution of derived ε , the average value will fluctuate greatly. This method models the antenna placement well, but the solving process makes it complicated and highly uncertain in many cases. For example, the hyperbola has small horizontal width, incomplete shapes, unclear vertex position, or is located in shallow layers. When the measurement point is within 1 m from the vertex, the maximum error of the calculated dielectric constant can reach 38.2% [25]

$$\frac{|x - \frac{L}{2} - x_1|}{\sqrt{h^2 + (x - \frac{L}{2} - x_1)^2}} - \sqrt{\varepsilon} \frac{|x_1|}{\sqrt{H^2 + x_1^2}} = 0 \quad (4)$$

$$\frac{|x + \frac{L}{2} - x_2|}{\sqrt{h^2 + (x + \frac{L}{2} - x_2)^2}} - \sqrt{\varepsilon} \frac{|x_2|}{\sqrt{H^2 + x_2^2}} = 0 \quad (5)$$

$$\frac{1}{\sqrt{\varepsilon}} \sqrt{h^2 + \left(x - \frac{L}{2} - x_1\right)^2} + \frac{1}{\sqrt{\varepsilon}} \sqrt{h^2 + \left(x + \frac{L}{2} - x_2\right)^2} + \sqrt{H^2 + x_1^2} + \sqrt{H^2 + x_2^2} - \frac{ct}{\sqrt{\varepsilon}} = 0 \quad (6)$$

$$\frac{h \sqrt{\varepsilon} \sin \theta}{\sqrt{1 - \varepsilon \sin^2 \theta}} + H \tan \theta - \frac{L}{2} = 0 \quad (7)$$

$$\frac{h}{\sqrt{1 - \varepsilon \sin^2 \theta}} + H \frac{\sqrt{\varepsilon}}{\cos \theta} - \frac{t_0 c}{2} = 0. \quad (8)$$

In summary, the first method is straightforward to solve but ignores the influences of the placement of the antenna, which causes estimation errors. The second and third methods have models close to a real-world scenario, but the complicated solving process brings errors. All ignore the object scale. Considering these factors, we propose a new approach to overcome the above problems while ensuring the accuracy of geometric modeling and the computational solution.

C. Proposed Method

Both the second and third methods have errors introduced in solving the equations for the implicit functions. These two methods need to determine the vertex position, so that it can be used as a known variable to reduce the set of parameters of the equations. However, it is difficult to obtain the precise vertex position and the deviation will lead to a calculation

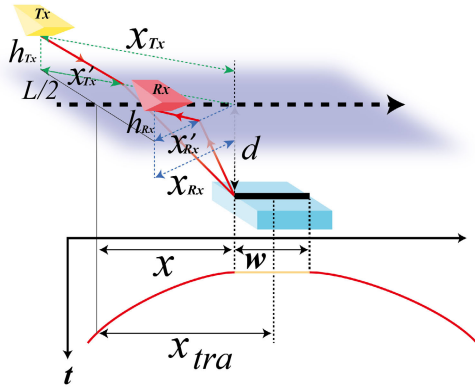


Fig. 4. RoPeR CH2 antenna position model.

error. Another issue is that the lookup table used by the second method has some pitfalls in describing the shape of the PSD. Therefore, we propose to use the form of vectors to express the PSD shape, which improves the accuracy of the solution and avoids nonunique solution problems. In addition, the height and spacing of the antenna are still considered in the modeling of our method.

For the Zhurong rover, the radar antenna is positioned in the vertical direction of the traveling path (see Fig. 4). Accordingly, we change the geometric modeling of the hyperbolic method to the following equations:

$$x_{Rx} = x_{Tx} \\ = \sqrt{x^2 + \left(\frac{L}{2}\right)^2} \quad (9)$$

$$\frac{x'_{Tx}}{\sqrt{h_{Tx}^2 + x'^2_{Tx}}} - \sqrt{\varepsilon} \frac{x_{Tx} - x'_{Tx}}{\sqrt{(x_{Tx} - x'_{Tx})^2 + d^2}} = 0 \quad (10)$$

$$\frac{x'_{Rx}}{\sqrt{h_{Rx}^2 + x'^2_{Rx}}} - \sqrt{\varepsilon} \frac{x_{Rx} - x'_{Rx}}{\sqrt{(x_{Rx} - x'_{Rx})^2 + d^2}} = 0 \quad (11)$$

$$\sqrt{h_{Tx}^2 + x'^2_{Tx}} + \sqrt{\varepsilon} \sqrt{(x_{Tx} - x'_{Tx})^2 + d^2} + \sqrt{h_{Rx}^2 + x'^2_{Rx}} + \sqrt{\varepsilon} \sqrt{(x_{Rx} - x'_{Rx})^2 + d^2} = ct \quad (12)$$

where x represents the horizontal distance between the rover and the object, x_{Tx} represents the horizontal distance between the Tx antenna and the object, h_{Tx} represents the height of the Tx antenna, 0.345 m in the TW-1 case, x_{Rx} represents the horizontal distance between Rx antenna and the object, and h_{Rx} represents the height of the Rx antenna, which is 0.306 m here. L is the spacing distance between Tx and Rx antenna, set as 0.42 m. d represents the object depth. Both x'_{Tx} and x'_{Rx} are the incidence and exit positions of electromagnetic waves with the ground.

Equations (9)–(12) do not model the size of the object. However, if the target size is not omittable, the scale should

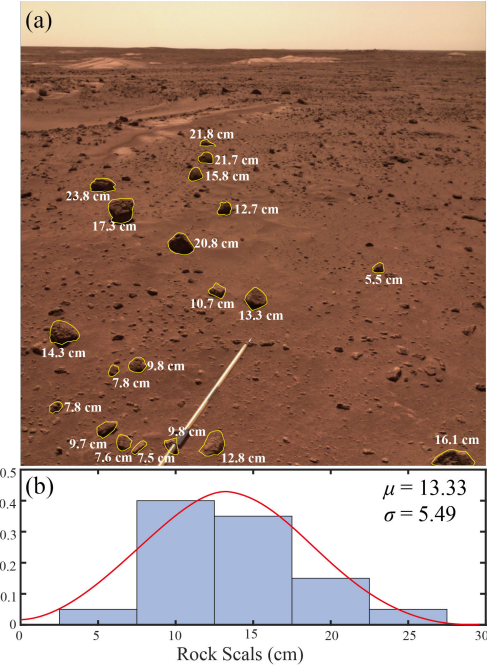


Fig. 5. Examples of surface rocks. (a) Image taken on day 73. (b) Rock scale histogram.

be considered. We approximate the subsurface object as a rectangle, causing the middle part of the hyperbola to be wider (see Fig. 4). Denote (9)–(12) as $t = f(x, d, \varepsilon)$. The equation after considering the width of the object becomes a segmented function, given by (13) and (14), where x_{tra} is the distance of the rover from the center of the object and w is the width of the object. Equation (14) means that the middle portion of the hyperbola is filled with the vertex value

$$t = f\left(|x_{tra}| - \frac{w}{2}, d, \varepsilon\right) \quad \left(|x_{tra}| > \frac{w}{2}\right) \quad (13)$$

$$t = f(0, d, \varepsilon) \quad \left(|x_{tra}| < \frac{w}{2}\right). \quad (14)$$

According to (9)–(14), optimization methods such as gradient descent and univariate search technique can be used for fitting. The three steps are: input the initial d_0 , w_0 , and ε_0 to get the hyperbolic shape, then calculate the error with the measurement points, and gradually adjust d_0 , w_0 , and ε_0 to reduce the error. However, this method has local optimal solutions and converges very slowly. Due to the dry Martian environment and the shallow detection depth of the CH2, the solution space of (ε, d) is not very large, making the enumeration method acceptable to obtain an optimum solution.

The size and the elements of the look-up matrix are determined according to the settings of the RoPeR and the properties of Martian subsurface materials. The width range of the general PSD hyperbola does not exceed 10 m, and the dielectric constant of the soil is between 1.1 and 10. The scanning interval of the RoPeR CH2 operation is 0.05 m. The detection depth of HF GPR will not exceed 20 m. Because of the lack of information on subsurface rock size, we set the width of rocks as a constant value of 15 cm, referring to the wavelength of CH2 and the scale of the rocks on the surface (see Fig. 5). The shape of the hyperbola can be calculated

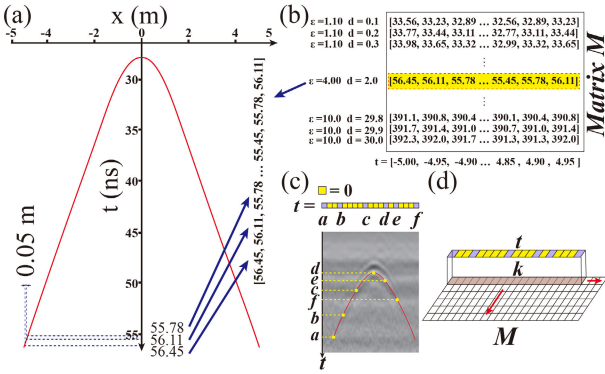


Fig. 6. (a) Example of PSD shape with $\varepsilon = 4$ and $d = 2$. (b) Matrices M contain all forward calculated hyperbolic shapes. (c) Representation of the measured points in B-scan in the vector t . (d) Schematic of the method using sliding windows.

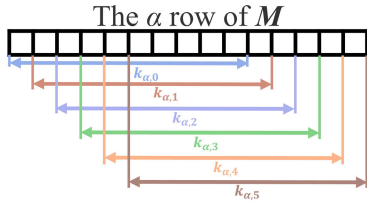


Fig. 7. Schematic representation of the mapping vector k during window sliding.

with (9)–(14). The interval of the dielectric constant is set as 0.01. The depth interval is set as 0.1 m. All possible shapes of the hyperbola are calculated and stored in the matrix M [see Fig. 6(b)]. The scale of matrix M is $w \times h$, which represents all the possible combinations of different depths and ε within the constraints of the range and intervals defined here. The vector t can be obtained by measuring the PSDs in the B-scan image. The length of vector t is n , the width of the measured hyperbola. Each element in the vector t represents the time t of each measurement point. The distance between every two adjacent elements in the vector t differs by 0.05 m. The elements of the vector t that are not located on the hyperbola are filled with zeros [see Fig. 6(c)]. The measurement vector t is searched in the matrix M using the sliding window method [see Fig. 6(d)]. When the window slides, the vector k is a map of t in M . So, the map vector k also has a length of n . The loss is defined as the mean square error (mse) between t and k . The column number of the smallest loss corresponds to the dielectric constant and depth of the PSD.

α and β represent the row and column coordinates of the starting point of the sliding window, respectively. The mapping vector $k_{\alpha,\beta}$ is given in (15) (see Fig. 7). α is in the range of $[1, h]$, and β is in the range of $[0, w - n]$. The loss $_{\alpha,\beta}$ is the deviation between $k_{\alpha,\beta}$ and t , obtained by (16). The loss $_{\alpha}$ represents the error in line α , which is calculated with (17). The one with the smallest error is the optimal solution. The line number α corresponds to the dielectric constant ε and depth d (18)

$$k_{\alpha,\beta} = M(\alpha, \beta : \beta + n) \quad (15)$$

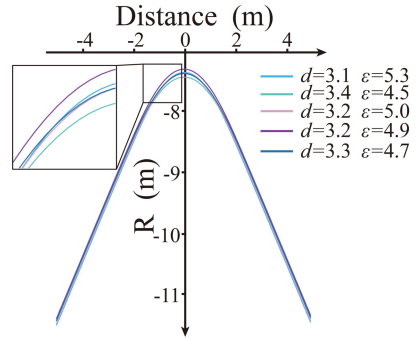


Fig. 8. Hyperbolas with different parameters but similar shapes.

$$\text{loss}_{\alpha,\beta} = \frac{1}{n} \sum (t - k_{\alpha,\beta})^2 \quad (16)$$

$$\text{loss}_{\alpha} = \min_{\alpha} (\text{loss}_{\alpha,0}, \text{loss}_{\alpha,1}, \dots, \text{loss}_{\alpha,w-n}) \quad (17)$$

$$\varepsilon, d \leftarrow \arg \min_{\alpha} (\text{loss}_1, \text{loss}_2, \dots, \text{loss}_h). \quad (18)$$

This lookup table method is similar to 2-D convolutional but replaces the “multiplying corresponding elements and summing” operation with calculating Euclidean distance between the data and kernel to identify the optimal solution location [36], [37], [38].

This work also uses a table searching method to find the solution, but instead of vertex position and eccentricity, vector form is used to represent the shape of the hyperbola, so that only clearly visible measurement points of the PSD are used for searching. Furthermore, the vertex point is easily interfered with by noises and interrupted/missed by switch operations of GPR. Also, in the case of an incomplete hyperbola, the dielectric constant can still be estimated based on measurement points at the hyperbola tail. Therefore, the proposed method can be applied to the case of incomplete hyperbolas and blurred vertices. Since a lookup table is used, the three issues of Method 3 described in Section II-B3 are avoided.

In addition, the deviations caused by noise points in the radargram are mitigated by setting a realistic range for the dielectric constant ε in the table. Also, the physical model considers both antenna height and spacing to ensure the completeness of the formula and improve the accuracy of the results.

D. Analysis of Errors

1) *Curve Similarity Analysis:* Different combinations of depth and dielectric constant ε can still result in similar shapes of the hyperbolas. Five pairs of dielectric constant and depth are listed in Fig. 8. The results of the forward calculations show that these curves have a high degree of similarity in shape, especially along their tails. The main difference among these five hyperbolas is the shape of the curve near the vertex position. Therefore, the measuring point should be close to the vertex position as much as possible to differentiate the effects of ε on the hyperbola. Here, we analyze the uncertainties caused by the similarity of the hyperbolic curves. Note that this type of error is unavoidable in all the mentioned hyperbola methods.

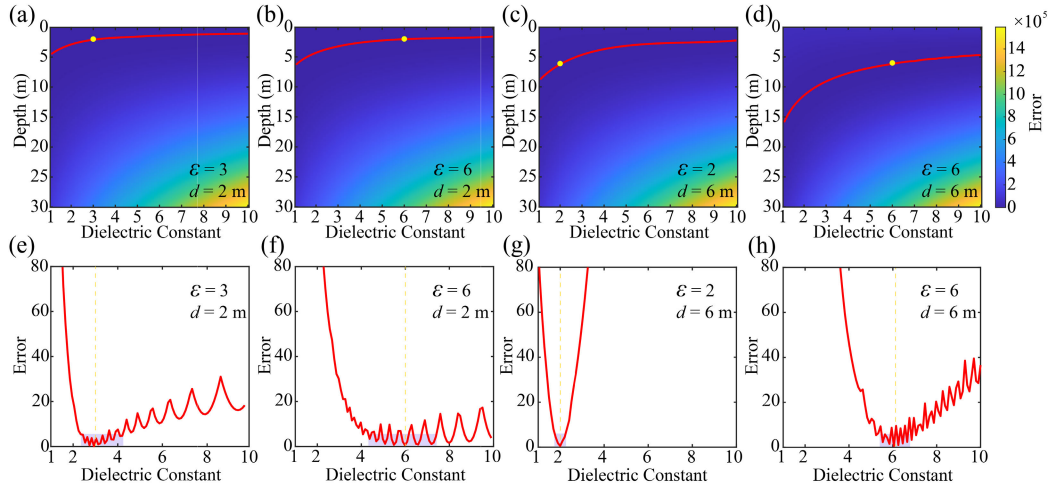


Fig. 9. (a)–(d) Similarity distribution map of different dielectric constants and depths. (e)–(h) Minimum deviation curves for different dielectric constants.

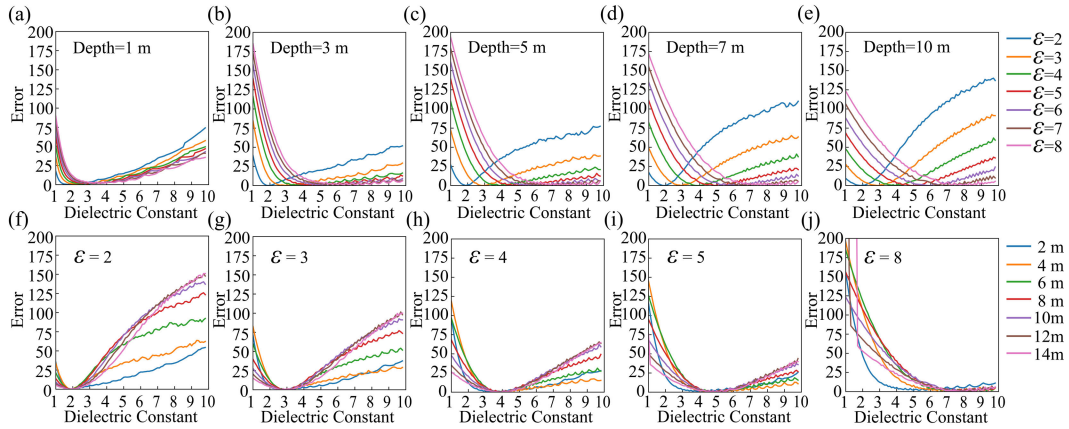


Fig. 10. Minimum deviation curves for (a)–(e) different depths and (f)–(j) dielectric constants.

We generated four cases of hyperbolic forms ($d = 2, \epsilon = 3$, $(d = 2, \epsilon = 6)$, $(d = 6, \epsilon = 2)$, and $(d = 6, \epsilon = 6)$) and calculated the corresponding mse of all the forward results to obtain the distribution map of similarity [see Fig. 9(a)–(d)]. The horizontal coordinate in the figure is the dielectric constant, the vertical coordinate is the depth, and the yellow points relate to the listed hyperbola. The color bar represents the similarity between the listed hyperbola and all the other possibilities. We also select the minimum value (meaning the most similar one) in each column to draw a red line in Fig. 9(a)–(d) to show the similarity between the listed hyperbola and those generated with different ϵ values.

By comparing Fig. 9(e) and (f) or Fig. 9(g) and (h), we could observe that at the same depth, the larger ϵ results in a more similar shape of hyperbola than the small ϵ . Fig. 10(a)–(e) shows the deviations of hyperbola shapes varying with ϵ at the depths of 1, 3, 5, 7, and 10 m. The hyperbola appearing in the shallow depth has higher similarity than those at depth. Regardless of the depth, it is consistent that the larger dielectric constant ϵ results in a more similarly shaped hyperbola. For example, when the listed hyperbola has $\epsilon \geq 5$ in Fig. 10(b)–(e), the deviation is low although ϵ varies in a large range. Fig. 10(f)–(j) gives the deviation curves changing with depth with a fixed dielectric constant of 2,

3, 4, 5, and 8, respectively. When the dielectric constant is large, e.g., 8, the difference in hyperbola morphology becomes very small. Generally, ϵ of Martian regolith/dust is much smaller than 8, but igneous rocks have relatively large ϵ .

Based on the observations, the following measurement strategies could be applied to improve the accuracy. When measuring the PSD, especially those in the shallow depth and potentially large ϵ area, measurement points should be marked as accurately as possible. As mentioned, another strategy is to select measurement points near the vertex position, which can be well adopted in the proposed method as only the parameters with the lowest deviation are selected. However, as in the method described in Section II-B3, the average error of measurement points within 1 m can reach 10%–38.2% [39].

2) *Measurement Points Selection:* As mentioned Section II-D1, the selection of measurement points will affect the accuracy of the results. Hence, we set up a selection range of measurement points for the hyperbola-shaped signal at different depths. In general, the horizontal width of the hyperbola in B-scan data is mainly related to factors, such as the radiation patterns of the antenna, attenuation, ϵ , the depth of the scatter, and so on. The horizontal width usually increases with the depth.

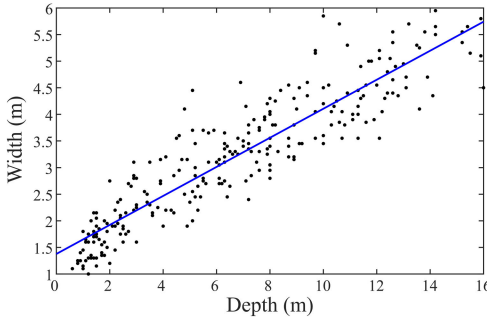


Fig. 11. Relationship between depth and horizontal width.

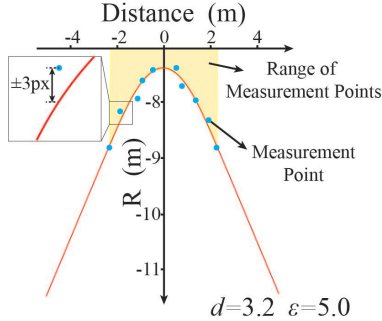


Fig. 12. Measurement point error test diagram.

The horizontal width usually increases with the depth as in Fig. 11, which shows the diagram of the depth and horizontal width of PSDs in RoPeR data. The relationship can be fitted as (19). Thus, the width range is set as the average width of the hyperbola at a certain depth

$$\text{Width} = 0.2728 * \text{depth} + 1.377. \quad (19)$$

When selecting a measurement point along the hyperbola-shaped signal, we only use those within the measurement width as illustrated by the yellow color in Fig. 12.

Based on the measurement results of the Apollo experiment, the density of soil increases with depth along with the dielectric constant [40]. The width of the hyperbola normally becomes wider with the increasing scale of the target. We set the object scale to 15 cm, acknowledging that objects in the subsurface could be much larger. Therefore, if an ideal model, e.g., (1), is used to fit the hyperbola produced by much larger objects, we will obtain a smaller ε . We remove the hyperbolas when the dielectric constant remains small at very deep depths, together with clear outliers at the same depth. When labeling hyperbolas, these cases are removed to mitigate interferences at the target scale.

3) Measurement Error: Here, we analyze the errors introduced in the measurement of hyperbolas. Since it is difficult to derive ε in terms of (x, t) directly using (9)–(14), we obtained the errors using statistical analysis. The measurement errors of the hyperbola are generated randomly within $[-3 \text{ pixels}, +3 \text{ pixels}]$, following a normal distribution. For RoPeR data, each pixel represents 0.1147 ns.

First, we obtain the hyperbola by forwarding calculation (9)–(14) and then select ten points randomly on the curve because a similar amount of measurement points are used during the manual selection process. Note that two of the

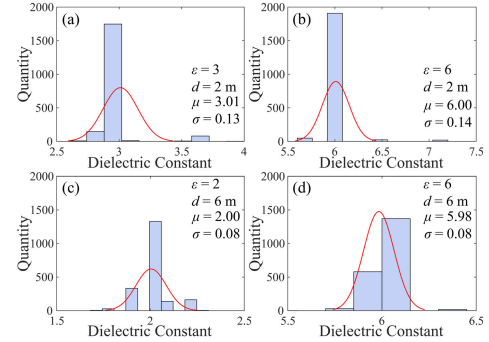


Fig. 13. Test results in the case of four combinations of dielectric constants and depths (a–d).

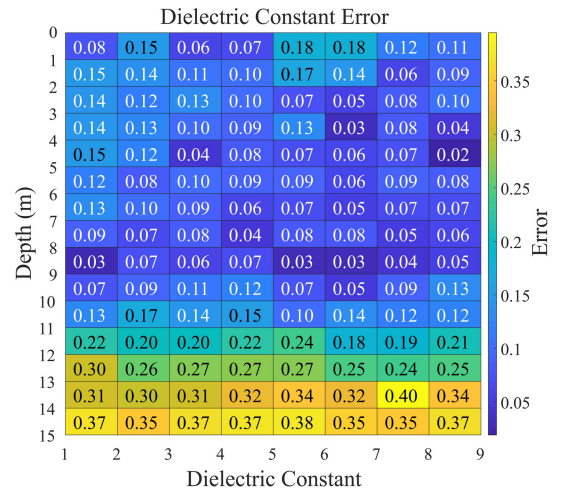


Fig. 14. Dielectric constant error distribution of hyperbola with different dielectric constants and depths.

measurement points are the left and right ends of the yellow area and the remaining eight points are randomly generated (see Fig. 12). Third, 2000 test cases for each combination of dielectric constants and depths (four examples are given in Fig. 13) are performed to estimate the error of ε . The histogram and the standard deviation of the dielectric constant results are given in Fig. 13.

According to Fig. 9(e)–(h), there are many local optima, which differ from the optimal solution. These local optimal solutions do not follow a normal distribution. Although the errors of the measurement points are normally distributed, the local optimal solution distribution also affects the distribution of the measurement results.

The measurement error of combinations of dielectric constant ranging from 1 to 9 and the depth ranging from 0 to 16 m is shown in Fig. 14. As can be seen from the error distribution, when the depth is less than 9 m, the average error can be kept below 5%, and when the depth is more than 10 m, the error increases sharply.

The difference in rock width also affects the measurement results. We set the rock widths as 0.25, 0.35, 0.45, and 0.55 m. Based on (9)–(14), we calculate the hyperbolic shape and then fit the curve using the rock width of 0.15 m; the results are shown in Fig. 15. With the rock size departing from the preset value, the fitting result of dielectric constant decreases

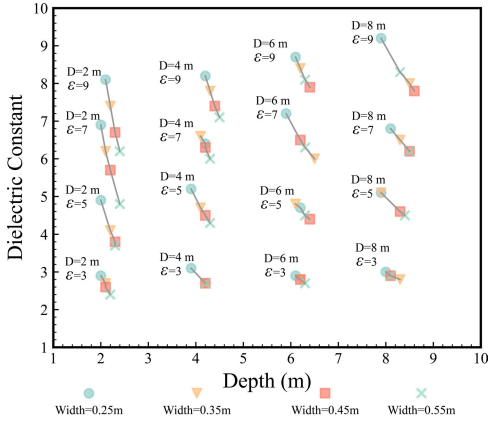


Fig. 15. Effect of rock width on measurement errors.

TABLE I
DIELECTRIC CONSTANT ERRORS CORRESPONDING
TO DIFFERENT ROCK SCALES

Methods	0.25 m	0.35 m	0.45 m	0.55 m	Average
Dielectric Constant Errors of Ignore Rock Width	8.8%	12.7%	15.0%	18.6%	13.8%
Dielectric Constant Errors of Rock Width 0.15 m	4.0%	9.4%	12.7%	15.0%	10.3%

and the derived depth increases compared to the actual value. The shallow region with a high dielectric constant is the most sensitive to the rock width. However, we rarely pick hyperbola in the shallow region (≤ 2 m).

By comparing the calculation results of methods with and without consideration of the scale of the rock (see Table I), it can be seen that including the width of the rock can reduce the calculation error. Using this approach, when the width of the rock is no larger than 0.55 m, the average error in measuring the dielectric constant is 10.3%. Considering the scale distribution of exposed rocks on the surface (as shown in Fig. 5) and the wavelength of CH2, the value of w used in (13) and (14) is set to 0.15 m. For rocks with a size larger than 0.55 m in the deeper region, the calculated depth results exceed the radar detection depth limit; thus, it is filtered out. Additionally, these results produce an arbitrarily low dielectric constant and are consequently removed.

4) *Evaluation With FDTD Simulations:* To verify the accuracy of the method in this article, we simulated the model of Fig. 4 using gprMax and set the subsurface object scale to 15 cm (see Fig. 16) [41].

The simulation results are computed by using the “fitting method ignoring antenna position and stone scale (cyan line),” “solving by table look-up method ignoring rock scale considering only antenna position (blue line),” and the method in this article (red line). The fitting results are shown in Table II.

From the comparison results, it can be seen that it is necessary to consider the antenna height. Not considering the object scale will make the dielectric constant calculation result small.

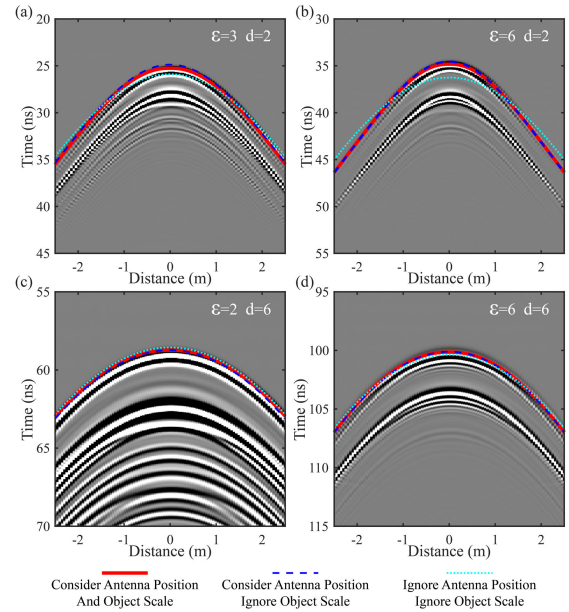


Fig. 16. gprMax simulation results with four combinations of dielectric constants and depths (a-d).

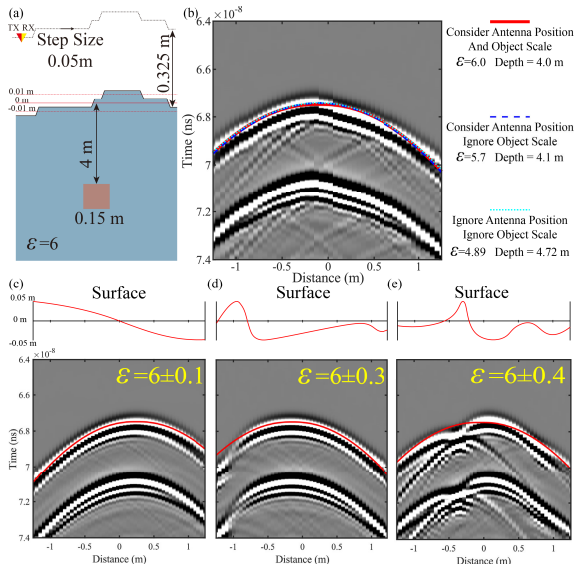


Fig. 17. (a) Simulation model. (b) Simulation results of different methods with the elevation data of the landing region. (c–e) Simulation results of three synthetic surface elevation models.

We also analyzed the measurement errors caused by uneven surfaces. We used the elevation data recorded by the radar during the rover travel to build simulation models using gprMax (see Fig. 17). The elevation profile shows that the surface of the traversing path is flat, with an undulation width of no more than 5 cm. Based on the simulation results, such undulations do not alter the results. To test further the reliability of the algorithm, we set up three different cases with maximum surface undulations of 0.1 m per simulation [see Fig. 17(c) and (d)]. Based on the results, the error was assessed to be below 7% by applying the algorithm used in this study.

Note that there might be additional errors caused by the differences in dielectric parameters of gigahertz level, the

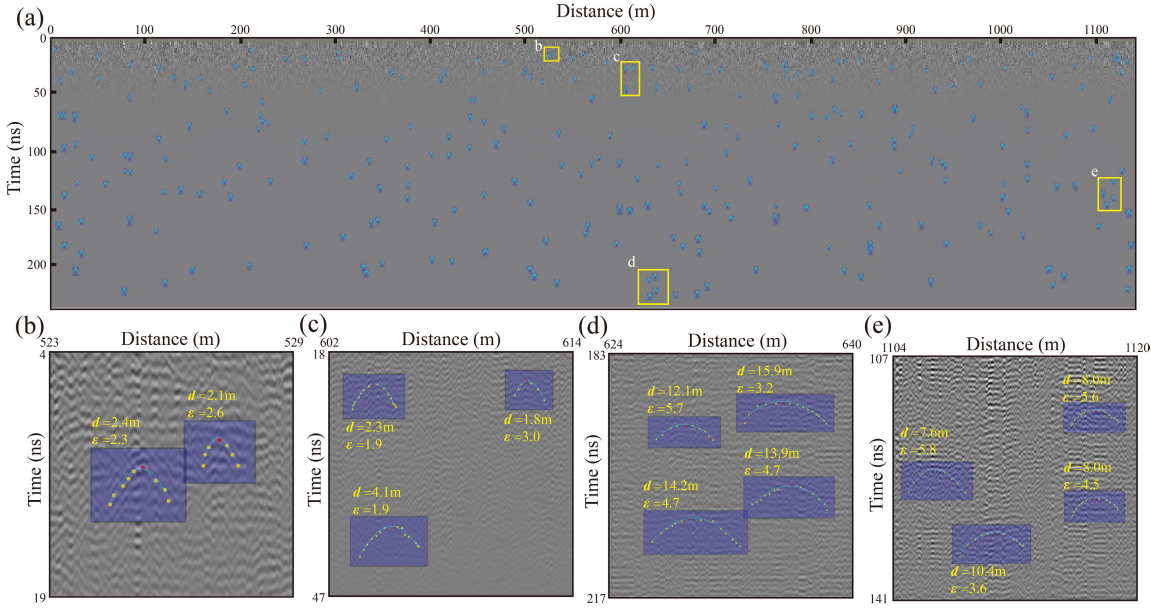


Fig. 18. (a) Labeled PSDs in GPR B-scan data. (b)–(e) Partial area display.

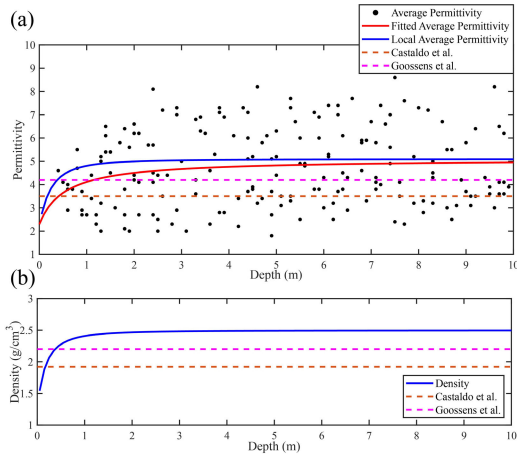


Fig. 19. (a) Estimated dielectric constants of 270 recognized scatters and the fitted line of dielectric constant versus depth. (b) Depth and density relationship.

TABLE II
COMPARISON OF SIMULATION DATA FITTING RESULTS

Simulation	Consider Antenna Position And Object Scale	Only Consider Antenna Position	Ignore Antenna Position And Object Scale
$d=2, \varepsilon=3$	$d=2.0, \varepsilon=3.0$	$d=2.0, \varepsilon=2.9$	$d=2.05, \varepsilon=2.94$
$d=2, \varepsilon=6$	$d=2.0, \varepsilon=6.0$	$d=2.0, \varepsilon=5.9$	$d=3.50, \varepsilon=2.71$
$d=6, \varepsilon=2$	$d=6.0, \varepsilon=2.0$	$d=6.0, \varepsilon=2.0$	$d=6.54, \varepsilon=1.94$
$d=6, \varepsilon=6$	$d=6.0, \varepsilon=6.0$	$d=6.1, \varepsilon=5.8$	$d=7.05, \varepsilon=4.76$
ε Error	0%	2.08%	20.1%

target shape, and so on, which are not analyzed here as they are not the focus of this study.

III. RESULTS

After deduplication, splicing, and signal enhancement, the final B-scan data of the RoPeR are shown in Fig. 18(a).

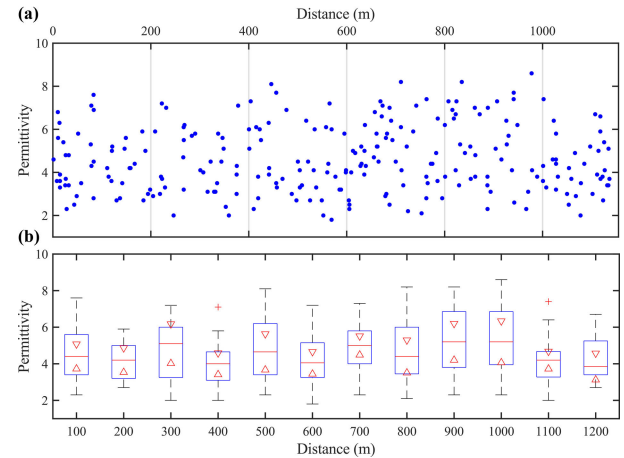


Fig. 20. (a) Distribution of dielectric constant and distance relationship. (b) Distribution of dielectric constants in different distance intervals.

The shallow subsurface structure (<16 m) of the UP area can be seen from the radar image. No obvious layered structure is observed in the surveyed area. The number of PSDs present in the data is relatively small compared to that at the CE-4 landing site. Moreover, the shape of the PSDs is interfered with by the noise, which also makes it more challenging in finding PSDs.

We employed the traditional manual labeling method to find 270 PSDs in the RoPeR image [see Fig. 18(a)]. When labeling the PSDs, we first determined the approximate location of the vertex, shown as a “red point” in Fig. 18(b)–(e). Then, the other measurement points of the PSD were marked (“yellow points”). When labeling a measurement point, the dielectric constant ε can be approximately derived from (1). Preliminary filtering of the hyperbola signal is performed by checking if ε lies within a reasonable value. After filtering, the dielectric constant and depth of the remaining PSDs are

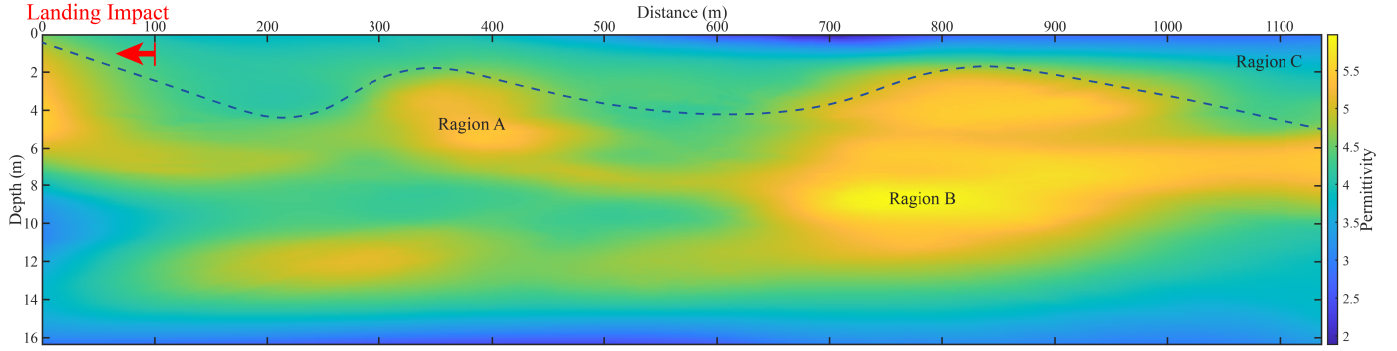


Fig. 21. Shallow surface distribution of dielectric constant.

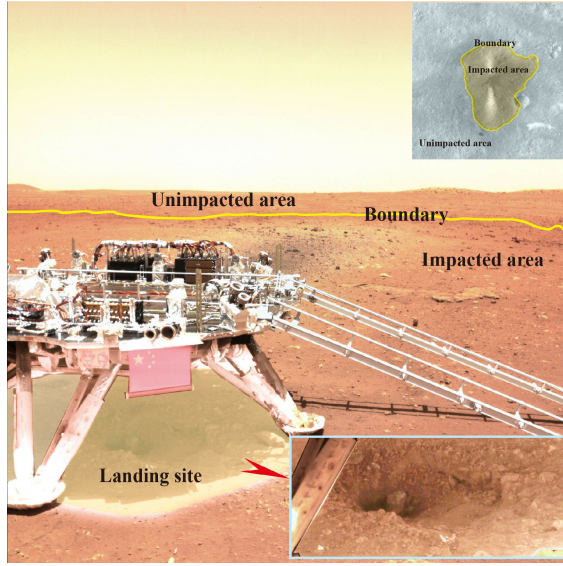


Fig. 22. Landing site images.

calculated according to the methodology presented in this article.

The blue hyperbola in Fig. 18(b)–(e) is the solution found by applying the methodology in this study. It can be seen that the hyperbola found from the table search is in good agreement with the PSD in B-scan. Moreover, the calculation results are not greatly affected by the uncertainties of a measurement point or vertex. The estimated dielectric constant from each subsurface boulder was obtained as marked by “black dots” in Fig. 19(a).

The estimated value with the hyperbola method is the average dielectric constant of the materials overlying the scatter [“red line” in Fig. 19(a)]. The local dielectric constant can be deduced from the depth and average constants of the two adjacent layers, according to the following equation [21], [42]:

$$\varepsilon_{n \sim n+1} = \frac{d_{n+1}\varepsilon_{n+1}\sqrt{\varepsilon_n} - d_n\varepsilon_n\sqrt{\varepsilon_{n+1}}}{d_{n+1}\sqrt{\varepsilon_n} - d_n\sqrt{\varepsilon_{n+1}}} \quad (20)$$

where n represents the index of the layer, the dielectric constant between n and $n+1$ layers is represented by $\varepsilon_{n \sim n+1}$, d_n represents the depth of the n th layer, and ε_n represents the dielectric constant of the n th layer. The obtained local dielectric constant versus depth is represented by the blue line

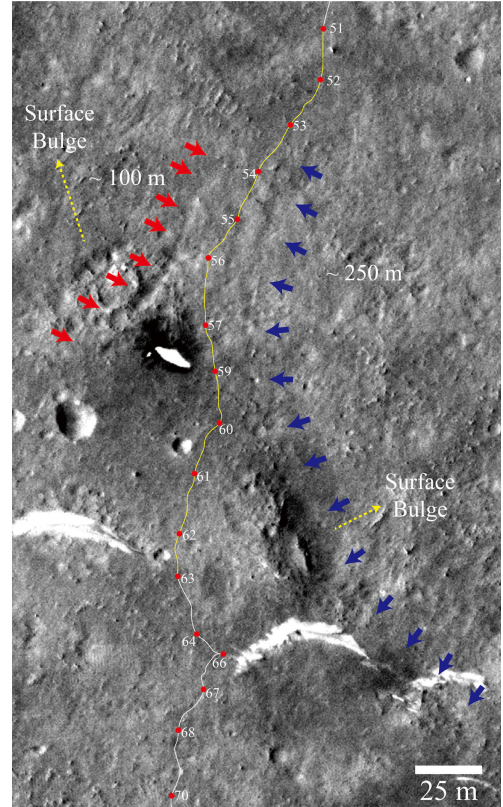


Fig. 23. HiRISE image of the rover driving at 300–500 m.

in Fig. 19(a), which is as follows:

$$\varepsilon = \frac{5.093d^2 + 3.897d + 0.4418}{d^2 + 0.7664d + 0.197}. \quad (21)$$

According to the relationship between the dielectric constant and density studied by Carrier III et al. [43], (22), the density at different depths can be calculated based on the regional dielectric constant [see Fig. 19(b)] [43]. The fitted relationship can be expressed as (23)

$$\rho = \frac{\ln \varepsilon}{\ln 1.919} \quad (22)$$

$$\rho = \frac{2.497d^2 + 2.03d + 0.174}{d^2 + 0.8132d + 0.1396}. \quad (23)$$

From the PSD calculated dielectric constants, we find that the shallow surface layer dielectric constants in the

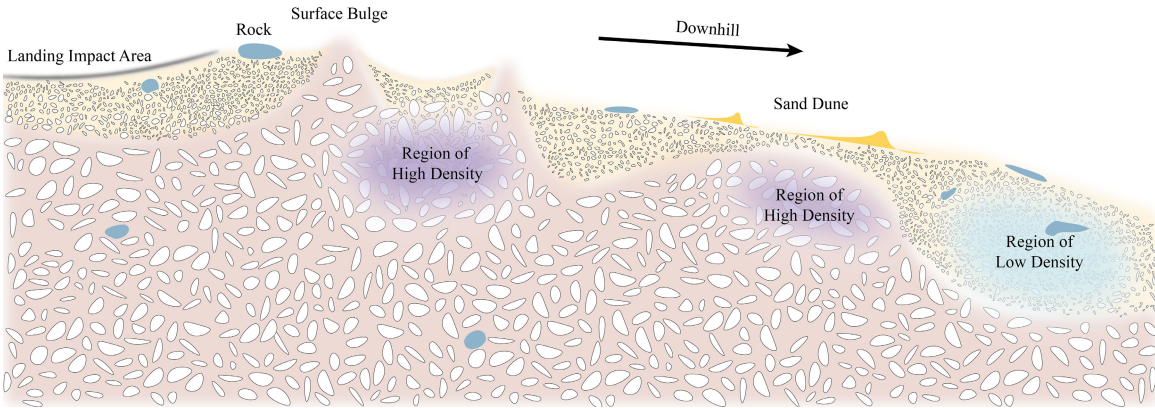


Fig. 24. Speculated geological structure picture (not in scale).

TW landing zone are distributed between 2 and 8. As the depth increases, the local dielectric constant gradually increases to 5.1 and the density reaches $2.5\text{g}/\text{cm}^3$. From the fitted curves of the dielectric constant and depth, we observe that the dielectric constant and density increase a little below the depth of 2 m. Castaldo et al. [2] calculated a surface dielectric constant of about 3–4 for the UP region based on SHARAD data. Goossens et al. [44] derived a soil density of 2–2.4 g/cm^3 in the UP area using the gravitational field model. Hence, our estimates at the depth are slightly higher than those from remote sensing observations. We also analyzed the dielectric constant variations with the traveling position [see Fig. 20(a)]. The distribution of the dielectric constant was calculated for each 100-m interval [see Fig. 20(b)]. The distribution of the dielectric constant is approximately the same over the whole area. The center of the distribution of the dielectric constant is around 4.5 in different intervals.

The 2-D distribution map along the depth and traveling distance of the dielectric constant are obtained by interpolating with the locally weighted scatter plot smooth (LOWESS) method (see Fig. 21) [45]. It suggests the heterogeneity of the shallow subsurface layer. Note that the signals of the radar image (see Fig. 17) concentrate in the upper part, while the ε map (see Fig. 20) reveals information as deep as 16 m. It demonstrates the capability of the proposed method to extract weak and incomplete PSD signals at depth. Based on the analysis in Sections II-D3 and II-D4, uncertainty is relatively high in the region deeper than 10 m.

IV. DISCUSSION

The radar image does not display obvious layering (see Fig. 18); however, the dielectric constant distribution map shows the changing of ε at the depth range of 2–5 m, marked as the blue line in Fig. 21. The navigation camera data show that there are sand dunes, loose dust, and debris covering the surface of the area. We presume that the material above this demarcation line is a mixture of loose, less dense regolith, and small debris.

As can be seen from the remote sensing image, an area with a radius of about 100 m near the landing site was eroded by the

lander jet plume [see Fig. 1(a)]. A small pit (enlarged view of Fig. 22) directly below the lander with an excavation depth of about 0.3 m was created during the landing. Influenced by aerodynamic forces, high temperatures, and other factors, a crater was formed below the lander (see Fig. 22). The elevation change of the rover's trace shows that the depth of the crater is about 0.5 m [see Fig. 1(c)]. Air currents during the landing exposed subsurface material, giving the surface a dark color.

The dielectric constant distribution map also demonstrates the change of ε (red arrows in Fig. 21) caused by the landing process within a horizontal distance of 100 m. The affected surface layer has a relatively high dielectric constant compared with the background within the depth of 1 m. During landing, the jets cause the migration of surface dust to the adjacent area exposing the underlying materials with higher ε or density.

Another region in the surface layer (0–4 m) showing a relatively low dielectric constant is Region C in Fig. 20 when the rover travels to 1000 m. The elevation of this area is also low, so the loose dust on the surface might have slid down and accumulated in this area causing low dielectric constant/density.

Fig. 23 shows the imaging data of the surface area of Region A. We can observe that two linear depression features appear on both sides of the driving track. The length of the left one (see Fig. 21 red arrow position) is 100 m and that of the right one (see Fig. 21 blue arrow position) is 250 m. At the tail part of both lines, bulge-like landforms with raised topography appear, which expose part of their basement. The linear depression could result from the collapse after the cooling of an intrusive igneous dike, and the bulge-like features could be exposed dike segments. Similar landforms have also been identified in eastern UP and proposed to represent dikes [46]. Moreover, the existence of dikes is also consistent with the density change of underground materials and an increased ε at Region A.

Another region with a high dielectric constant of 5–6 in the shallow surface layer is at the depth of 8–13 m (region B in Fig. 21). As can be seen from the elevation of the traversing path [see Fig. 1(c)], region B is in a sloping area and right

before the relatively large drop of the elevation indicated by the green arrows of Fig. 1(a) and (b). However, we did not observe the obvious connection between the subsurface region B and the surface geomorphology. The change in the surface height of region B might be caused by the collapse of the original landform, which could be related to the high density of the subsurface materials. Based on the dielectric constant distribution and image of the surface terrain and elevation, a model of the subsurface structure of the surveying area is shown in Fig. 24.

V. CONCLUSION

The in situ measurements of the Mars RoPeR onboard the Zhurong rover provide a rare opportunity to map the high-resolution subsurface stratigraphy in the southern Utopia area. The hyperbola method is the mainstream and effective approach to extract the dielectric constant distribution of the substance based on the diffraction signals in the radar image. In this study, we discuss the limitations of previous methods and propose a new approach that can adopt the accurate geometric model and address problems caused by its complexity. We also analyze the factors contributing to measurement errors and design strategies for selecting measurement points from the hyperbola signals to reduce errors. The errors of the proposed method under different conditions were estimated with statistical analysis. The results show that the average error can be less than 5% when the depth is less than 9 m.

The proposed method is applied to the RoPeR HF data. We extract 270 PSDs and estimated their dielectric constants ϵ to obtain the ϵ distribution map of the depth up to 16 m. The range of average dielectric constant is 2–8, and the Martian soil density below 2 m is about 2.5 g/cm^3 . The depth profile shows that ϵ increases little below 2 m. In the dielectric constant distribution map, we can see the clear impact of the jet plume in the landing process, reducing ϵ and density of the surface materials. The stratification appears at the depth of 2–5 m due to a change in ϵ . Two areas of relatively high ϵ below the depth of 4 m indicate the heterogeneity of materials in the shallow subsurface.

REFERENCES

- [1] C. M. Stuurman et al., "SHARAD detection and characterization of subsurface water ice deposits in utopia Planitia, Mars," *Geophys. Res. Lett.*, vol. 43, no. 18, pp. 9484–9491, Sep. 2016, doi: [10.1002/2016GL070138](https://doi.org/10.1002/2016GL070138).
- [2] L. Castaldo, D. Mège, J. Gurgurewicz, R. Orosei, and G. Alberti, "Global permittivity mapping of the Martian surface from SHARAD," *Earth Planet. Sci. Lett.*, vol. 462, pp. 55–65, Mar. 2017, doi: [10.1016/j.epsl.2017.01.012](https://doi.org/10.1016/j.epsl.2017.01.012).
- [3] E. S. Shoemaker, L. M. Carter, W. B. Garry, G. A. Morgan, and J. J. Plaut, "New insights into subsurface stratigraphy Northwest of Ascraeus Mons, Mars, using the SHARAD and MARSIS radar sounders," *J. Geophys. Res., Planets*, vol. 127, no. 6, Jun. 2022, Art. no. e2022JE007210.
- [4] L. M. Carter et al., "Shallow radar (SHARAD) sounding observations of the medusae fossae formation, Mars," *Icarus*, vol. 199, no. 2, pp. 295–302, 2009.
- [5] Y. Zou et al., "Scientific objectives and payloads of Tianwen-1, China's first Mars exploration mission," *Adv. Space Res.*, vol. 67, no. 2, pp. 812–823, 2021.
- [6] M. L. Searls, W. B. Banerdt, and R. J. Phillips, "Utopia and Hellas basins, Mars: Twins separated at birth," *J. Geophys. Res.*, vol. 111, no. E8, pp. 1–13, 2006.
- [7] M. M. Mills, A. S. McEwen, and C. H. Okubo, "A preliminary regional geomorphologic map in utopia Planitia of the Tianwen-1 Zhurong landing region," *Geophys. Res. Lett.*, vol. 48, no. 18, Sep. 2021, Art. no. e2021GL094629.
- [8] P. Brož and E. Hauber, "Hydrovolcanic tuff rings and cones as indicators for phreatomagmatic explosive eruptions on Mars," *J. Geophys. Res., Planets*, vol. 118, no. 8, pp. 1656–1675, Aug. 2013.
- [9] G. Picardi et al., "Performance and surface scattering models for the Mars Advanced Radar for Subsurface and Ionosphere Sounding (MARSIS)," *Planet. Space Sci.*, vol. 52, nos. 1–3, pp. 149–156, 2004.
- [10] J. Mouginot, A. Pommerol, P. Beck, W. Kofman, and S. M. Clifford, "Dielectric map of the Martian northern Hemisphere and the nature of plain filling materials: Dielectric map of Mars," *Geophys. Res. Lett.*, vol. 39, no. 2, Jan. 2012, Art. no. L02202, doi: [10.1029/2011GL050286](https://doi.org/10.1029/2011GL050286).
- [11] R. Seu et al., "SHARAD sounding radar on the Mars reconnaissance orbiter," *J. Geophys. Res.*, vol. 112, no. E5, pp. 1–18, 2007.
- [12] L. Ding et al., "Surface characteristics of the Zhurong Mars rover traverse at utopia Planitia," *Nature Geosci.*, vol. 15, no. 3, pp. 171–176, Mar. 2022.
- [13] J. Lai et al., "Comparison of dielectric properties and structure of lunar regolith at Chang'e-3 and Chang'e-4 landing sites revealed by ground-penetrating radar," *Geophys. Res. Lett.*, vol. 46, no. 22, pp. 12783–12793, Nov. 2019, doi: [10.1029/2019GL084458](https://doi.org/10.1029/2019GL084458).
- [14] Z. Dong, G. Fang, D. Zhao, B. Zhou, Y. Gao, and Y. Ji, "Dielectric properties of lunar subsurface materials," *Geophys. Res. Lett.*, vol. 47, no. 22, Nov. 2020, doi: [10.1029/2020GL089264](https://doi.org/10.1029/2020GL089264).
- [15] W. Fa, "Bulk density of the lunar regolith at the Chang'E-3 landing site as estimated from lunar penetrating radar," *Earth Space Sci.*, vol. 7, no. 2, Feb. 2020, Art. no. e2019EA000801, doi: [10.1029/2019EA000801](https://doi.org/10.1029/2019EA000801).
- [16] R. Wang et al., "A novel approach for permittivity estimation of lunar regolith using the lunar penetrating radar onboard Chang'E-4 rover," *Remote Sens.*, vol. 13, no. 18, p. 3679, Sep. 2021, doi: [10.3390/rs13183679](https://doi.org/10.3390/rs13183679).
- [17] S.-E. Hamran et al., "Radar Imager for Mars' subsurface experiment—RIMFAX," *Space Sci. Rev.*, vol. 216, no. 8, pp. 1–39, Dec. 2020.
- [18] T. M. Casademont et al., "Dielectric permittivity and density of the shallow Martian subsurface in Jezero Crater," *LPI Contrib.*, vol. 2678, p. 1513, Mar. 2022.
- [19] K. Rejšek et al., "A methodological contribution to use of ground-penetrating radar (GPR) as a tool for monitoring contamination of urban soils with road salt," *Urban Ecosyst.*, vol. 18, no. 1, pp. 169–188, Mar. 2015, doi: [10.1007/s11252-014-0391-y](https://doi.org/10.1007/s11252-014-0391-y).
- [20] A. Klotzsche, F. Jonard, M. C. Looms, J. Van Der Kruk, and J. A. Huisman, "Measuring soil water content with ground penetrating radar: A decade of progress," *Vadose Zone J.*, vol. 17, no. 1, pp. 1–9, Jan. 2018, doi: [10.2136/vzj2018.03.0052](https://doi.org/10.2136/vzj2018.03.0052).
- [21] C. H. Dix, "Seismic velocities from surface measurements," *Geophysics*, vol. 20, no. 1, pp. 68–86, Jan. 1955.
- [22] S. Shihab and W. Al-Nuaimy, "Radius estimation for cylindrical objects detected by ground penetrating radar," *Subsurface Sens. Technol. Appl.*, vol. 6, no. 2, pp. 151–166, Apr. 2005, doi: [10.1007/s11220-005-0004-1](https://doi.org/10.1007/s11220-005-0004-1).
- [23] I. Giannakis, F. Zhou, C. Warren, and A. Giannopoulos, "On the limitations of hyperbola fitting for estimating the radius of cylindrical targets in nondestructive testing and utility detection," *IEEE Geosci. Remote Sens. Lett.*, vol. 19, pp. 1–5, 2022, doi: [10.1109/LGRS.2022.3195947](https://doi.org/10.1109/LGRS.2022.3195947).
- [24] R. Persico et al., "Effect of the height of the observation line on the diffraction curve in GPR prospecting," *Near Surf. Geophys.*, vol. 13, no. 3, pp. 243–252, Jun. 2015, doi: [10.3997/1873-0604.2014042](https://doi.org/10.3997/1873-0604.2014042).
- [25] C. Rappaport, "A simple approximation of transmitted wavefront shape from point sources above lossy half spaces," in *Proc. IEEE Int. Geosci. Remote Sens. Symp. (IGARSS)*, Anchorage, AK, USA, Jun. 2004, pp. 421–424, doi: [10.1109/IGARSS.2004.1369052](https://doi.org/10.1109/IGARSS.2004.1369052).
- [26] C. M. Rappaport, "Accurate determination of underground GPR wavefront and B-scan shape from above-ground point sources," *IEEE Trans. Geosci. Remote Sens.*, vol. 45, no. 8, pp. 2429–2434, Aug. 2007, doi: [10.1109/TGRS.2007.901004](https://doi.org/10.1109/TGRS.2007.901004).
- [27] C. Rappaport, "A novel, non-iterative, analytic method to find the surface refraction point for air-coupled ground penetrating radar," in *Proc. 5th Eur. Conf. Antennas Propag. (EUCAP)*, 2011, pp. 1786–1789.
- [28] S. Liu et al., "Data pre-processing and signal analysis of Tianwen-1 rover penetrating radar," *Remote Sens.*, vol. 15, no. 4, p. 966, Feb. 2023, doi: [10.3390/rs15040966](https://doi.org/10.3390/rs15040966).

- [29] I. Giannakis, J. Martin-Torres, M.-P. Zorzano, Y. Su, C. Warren, and A. Giannopoulos, "Stochastic hyperbola fitting, probabilistic inversion, reverse-time migration and clustering: A novel interpretation toolbox for in-situ planetary radar," *Icarus*, vol. 400, Aug. 2023, Art. no. 115555, doi: [10.1016/j.icarus.2023.115555](https://doi.org/10.1016/j.icarus.2023.115555).
- [30] B. Zhou et al., "The Mars rover subsurface penetrating radar onboard China's Mars 2020 mission," *Earth Planet. Phys.*, vol. 4, no. 4, pp. 1–10, 2020, doi: [10.26464/epp2020054](https://doi.org/10.26464/epp2020054).
- [31] J. Feng, Y. Su, C. Ding, S. Xing, S. Dai, and Y. Zou, "Dielectric properties estimation of the lunar regolith at CE-3 landing site using lunar penetrating radar data," *Icarus*, vol. 284, pp. 424–430, Mar. 2017.
- [32] S. Boyd, S. P. Boyd, and L. Vandenberghe, *Convex Optimization*. Cambridge, U.K.: Cambridge Univ. Press, 2004.
- [33] N. Oudart, V. Ciarletti, A. Le Gall, Y. Hervé, and E. Brighi, "Retrieval of the ground dielectric permittivity by planetary GPR accommodated on a rover: Application to the estimation of the reflectors' depth by the WISDOM/ExoMars radar," *Planet. Space Sci.*, vol. 224, Dec. 2022, Art. no. 105606, doi: [10.1016/j.pss.2022.105606](https://doi.org/10.1016/j.pss.2022.105606).
- [34] R. I. Jennrich and M. L. Ralston, "Fitting nonlinear models to data," *Annu. Rev. Biophys. Bioeng.*, vol. 8, no. 1, pp. 195–238, Jun. 1979, doi: [10.1146/annurev.bb.08.060179.001211](https://doi.org/10.1146/annurev.bb.08.060179.001211).
- [35] G. Zhang, D. Allaire, and J. Cagan, "Taking the guess work out of the initial guess: A solution interval method for least-squares parameter estimation in nonlinear models," *J. Comput. Inf. Sci. Eng.*, vol. 21, no. 2, Apr. 2021, Art. no. 021011, doi: [10.1115/1.4048811](https://doi.org/10.1115/1.4048811).
- [36] K. Ghiasi-Shirazi, "Generalizing the convolution operator in convolutional neural networks," *Neural Process. Lett.*, vol. 50, no. 3, pp. 2627–2646, Dec. 2019, doi: [10.1007/s11063-019-10043-7](https://doi.org/10.1007/s11063-019-10043-7).
- [37] M. Aigner and S. Axler, *A Course in Enumeration* (Graduate Texts in Mathematics), vol. 238. Berlin, Germany: Springer, 2007, doi: [10.1007/978-3-540-39035-0](https://doi.org/10.1007/978-3-540-39035-0).
- [38] P.-E. Danielsson, "Euclidean distance mapping," *Comput. Graph. Image Process.*, vol. 14, no. 3, pp. 227–248, 1980, doi: [10.1016/0146-664X\(80\)90054-4](https://doi.org/10.1016/0146-664X(80)90054-4).
- [39] R.-G. Wang et al., "Study on the influencing factors of the permittivity estimation method considering antenna layout based on lunar penetrating radar," *Res. Astron. Astrophys.*, vol. 22, no. 10, Oct. 2022, Art. no. 105002.
- [40] G. H. Heiken, D. T. Vaniman, and B. M. French. (1991). *Lunar Sourcebook, A User's Guide to the Moon*. Accessed: Mar. 15, 2023. [Online]. Available: <https://ui.adsabs.harvard.edu/abs/1991lsug.book....H>
- [41] C. Warren, A. Giannopoulos, and I. Giannakis, "gprMax: Open source software to simulate electromagnetic wave propagation for ground penetrating radar," *Comput. Phys. Commun.*, vol. 209, pp. 163–170, Dec. 2016, doi: [10.1016/j.cpc.2016.08.020](https://doi.org/10.1016/j.cpc.2016.08.020).
- [42] J. H. Bradford, "Wave field migration as a tool for estimating spatially continuous radar velocity and water content in glaciers," *Geophys. Res. Lett.*, vol. 32, no. 8, 2005, Art. no. L08502, doi: [10.1029/2004GL021770](https://doi.org/10.1029/2004GL021770).
- [43] *Lunar Sourcebook, A User's Guide to the Moon*. Cambridge, U.K.: Cambridge Univ. Press, 1991, pp. 475–594.
- [44] S. Goossens, T. J. Sabaka, A. Genova, E. Mazarico, J. B. Nicholas, and G. A. Neumann, "Evidence for a low bulk crustal density for Mars from gravity and topography," *Geophys. Res. Lett.*, vol. 44, no. 15, pp. 7686–7694, Aug. 2017.
- [45] W. S. Cleveland, "Robust locally weighted regression and smoothing scatterplots," *J. Amer. Stat. Assoc.*, vol. 74, no. 368, pp. 829–836, 1979.
- [46] G. B. M. Pedersen, J. W. Head, and L. Wilson, "Formation, erosion and exposure of early Amazonian dikes, dike swarms and possible subglacial eruptions in the Elysium Rise/Utopia Basin region, Mars," *Earth Planet. Sci. Lett.*, vol. 294, nos. 3–4, pp. 424–439, Jun. 2010, doi: [10.1016/j.epsl.2009.08.010](https://doi.org/10.1016/j.epsl.2009.08.010).



Renrui Liu received the B.S. degree in optoelectronic information science and engineering from the School of Physics and Optoelectronic Engineering, Shandong University of Technology, Zibo, China, in 2020, and the M.S. degree in space big data analytics from the State Key Laboratory of Lunar and Planetary Sciences, Macau University of Science and Technology, Macau, China, in 2022, where he is currently pursuing the Ph.D. degree.

His research interests include deep learning, 3-D modeling, image processing, and ground penetrating radar (GPR) data processing.



Yi Xu (Member, IEEE) received the Ph.D. degree in electrical and computer engineering from the University of Pittsburgh, Pittsburgh, PA, USA, in 2012.

She is currently an Associate Professor with the State Key Laboratory of Lunar and Planetary Sciences, Macau University of Science and Technology, Macau, China. Her research interests include data processing and analysis of satellite microwave and radar, thermal modeling, and nanophotonic network architecture.

Dr. Xu is a member of the Association for Computing Machinery (ACM).



Ruonan Chen received the Ph.D. degree in Earth and planetary sciences from the Macau University of Science and Technology, Macau, China, in 2022.

She is currently the Research Scientist (A) of Temasek Laboratories, National University of Singapore, Singapore. Her research interests include computational electromagnetics and radar signal processing and imaging.



Jiannan Zhao received the Ph.D. degree in planetary geology and comparative planetology from the China University of Geosciences, Wuhan, China, in 2017.

He is currently an Associate Professor with the Key Laboratory of Geological Survey and Evaluation, Ministry of Education, China University of Geosciences. His research interests include geomorphology, mineralogy, and chronology of the Moon and Mars, focusing on Martian hydrologic activity.



Xiaoting Xu received the B.S. degree in geographic information systems from Yunnan Normal University, Kunming, China, in 2016, and the M.S. degree from the State Key Laboratory of Lunar and Planetary Sciences, Macau University of Science and Technology, Macau, China, in 2020, where she is currently pursuing the Ph.D. degree.

Her research interests include planetary subsurface sounding radar and planetary surface terrain analysis.